

Modelling Planetary Climate

Mihir Dasgupta

Feb-Jun 2021

Abstract

This report aims to evaluate 0d and 1d methods of modelling planetary climate and energetics via key thermal quantities (OLR, temperature profiles, etc.). We begin with a clear identification of the energy sources and sinks that drive atmospheric dynamics. A 0d model is developed to demonstrate the extent of its inaccuracy for a thermal profile of a spatially-averaged Earth system. However, the following section extends 0d techniques to a method to solve the Goldilocks problem in habitability. Section 4 looks at the mathematical representation of the atmospheric system, setting up numerous techniques used for our 1d models. Our radiative transfer model defines key variables that account for atmospheric interferences and evaluates the relationships between them. Section 6's radiative equilibrium model considers the evolution of certain variables as the system approaches equilibrium, stopping variables, and key equilibrium/output profiles. Our RCE model provides an addendum to its predecessor, adding a convective component, with profiles being generated to evaluate the effects convection has on the radiative equilibrium system.

Written under the direction of Ass. Prof. Joy Merwin Monteiro, Indian Institute of Science Education and Research – Pune (IISER-Pune). The Python programs used to develop all profiles in this report are currently hosted on [this](#) Github repository.

1 Examining Energy Sources and Sinks

The first step to understanding a climate model's working is to identify the energy sources and sinks that drive the system. Here, we will look at Earth as an example of a planetary system and examine its sources and sinks.

An energy source adds energy to the Earth system. There are a wide selection of potential sources that we will consider in this section. The concentration of matter at the Earth's core creates heat as a result of its displacement towards the planet's gravitational core [Ernst et al., 2016]: the conversion of gravitational potential to thermal energy occurs as the distance between the observed matter and the Earth's core falls. The collapse of matter during the formation of the planet released this energy as high levels of heat. However, these dynamics have evolved into an internal circulation underneath the Earth's crust as the surface hardened [Condie, 2013]. Therefore, any emitted energy as a result of sinking matter was transferred to the upward displacement of matter rising from the core -reflected by an increase in gravitational potential. The system formed a closed circulation that, today, does not significantly affect surface dynamics or

temperatures. As a result, we can assume its influence on the Earth's energy budget is negligible and disregard its impact on this scope of discussion.

The decay of radioactive heavy metals in the Earth's inner core releases high levels of energy [Turcotte and Schubert, 2002] that serve as one of the primary energy sources of the Earth's interior's dynamics. However, its impact on surface heating is dwarfed by that of insolation (0.03% of total energy budget [Archer, 2011]). Additionally, the impact of solar and lunar tides can cause heating in the climate system. Their gravitational forces exerted on the Earth (and vice-versa) induce tidal bulges as the Earth system is distorted (eg. oceanic tides). These bulges act as friction to the Earth's rotation, reducing its torque [Camuffo, 2001]. The energy lost in rotation is converted to thermal energy in the asthenosphere. However, the crust acts as an insulator to the effects of both tidal friction and radioactive decay [Lenardic et al., 2005]. It follows that these effects are often negligible on most other terrestrial planets as well. Therefore, the crust's presence reduces the influence of the internal energy of the Earth on the climate system - we can ignore their influence on the Earth's energy budget as we did the circulation of matter

in the Earth’s interior.

The remaining source of interest is incoming solar radiation, or insolation for short. The Sun remains the largest energy source on the Earth’s climate system as it exists today. Thus, the following models will primarily consider only insolation an energy source to maintain their inherent simplicity.

We now concern ourselves with identifying the energy sinks in the system i.e. the mechanisms by which the system loses energy. As the Earth’s interior acts as a source of energy, it follows that it cannot act as a sink. This narrows our focus to the mechanisms that allow the system to lose energy outside the planetary body.

One possibility is the loss of kinetic energy by the removal of matter from the system. Focusing on the Earth, this mass could be lost from particles in the atmosphere, more likely than anything else. However, the loss of matter from the atmosphere is negligible due to the strength of the Earth’s gravitational field, derived from the planet’s mass. Kinetic dissipation amounts to a mere 10 W/m^2 from the troposphere [Holopainen, 1963]. The other sink we can consider is the radiation emitted from the Earth’s surface. This acts as the primary energy sink in our climate system, and will be the main sink we consider in following models.

The importance of clearly identifying sources and sinks is paramount. By understanding the mechanisms by which energy is gained or lost from the system, we understand the stability of the system. It rests on the premise of a balanced energy budget (where there is no net energy input or output to or from the system). An imbalance in the budget would ultimately lead to the complete vaporization or freezing of the body, over monumental timescales. A predictable climate, and even the plausibility of habitability and the evolution of life, rest on this stability.

2 The Zero-Dimensional (0D) Model

This model is a member of the ‘Energy Balance Models’ classification, or EBM. These simple climate models attempt to predict the surface temperature of the Earth, considering all reasonable energy sources and sinks to do so. However, they do not concern themselves with resolving any dynamics of the climate system (as GCMs, or general circulation models, do). Most cli-

mate dynamics stem from an imbalance in energy distributions- here, creating temperature differences. On Earth, these temperature differences (primarily seen across the latitudinal axis) resolve themselves mainly via the oceanic and atmospheric circulation systems. EBMs deal with the energy balance of the system instead.

The zero-dimensional model is the simplest member of the EBM family. It views the Earth as an arbitrary, singular point in space, as if observed from an infinite distance. In this case, we ignore any spatial variation and remove all real coordinates from the x, y and z axes. The absence of any points of observation across altitude leads us to ignore the interference of an atmosphere in our energy budget. This simplifies our calculations significantly, as we no longer account for any atmospheric phenomena that could affect radiation incident on the planetary surface. The only variables to account for are the energy incident on the surface and the energy emitted by it, as was explained in the previous section on energy sources and sinks.

Note that `symp1` [Monteiro et al., 2018], `CLiMT` [Monteiro and Caballero, 2016], and `datetime` are the primary Python modules to solve for a stable surface temperature and will be used for later models.

2.1 Evaluating Absorptivity and Emissivity

A remaining quantity of interest is the average albedo(α) of the planetary surface. Figure 1’s model sets up the parameters that we will use to demonstrate how albedo could be calculated.

The solar constant (solar energy flux density), S has been approximated to 1376.6 W/m^2 [Johnson, 1954]. Viewed from the Sun, the planetary surface appears as a disk with surface area πR^2 . If the surface reflects a certain fraction (α) of all incident radiation, we can account for its influence. Therefore, we can model the total radiation incident on the surface by the expression, $\pi R^2 S(1 - \alpha)$.

The Stefan-Boltzmann law provides us with a framework with which we can estimate Earth’s emitted radiative flux (ϕT^4), where T is the equilibrium temperature that was calculated as the `surface_temperature` tendency in Figure 1, and $\phi \sim 5.68 \cdot 10^{-8} \text{ W/m}^2 \text{K}^4$.

The nature of the Earth’s surface plays a hand in reducing the emissivity of the planet. The Stefan-Boltzmann approximations make the false assumption of a blackbody surface, which ab-

sorbs (and thus, emits) all radiation incident on the surface. We accommodate for this difference by multiplying the approximation by a dimensionless ratio coefficient, ϵ , where $0 < \epsilon < 1$. Note that it is numerically equivalent to an absorption coefficient, as per Kirchhoff's thermal radiation law. Accounting for the rotational surface area, we model the aggregate emitted radiation as $4\pi R^2 \epsilon \phi T^4$.

The incoming and outgoing radiation must be equal to ensure a steady climate state. Thus,

$$4\pi R^2 \epsilon \phi T^4 = \pi R^2 S(1 - \alpha) \quad (1)$$

Simplifying,

$$\frac{S}{4}(1 - \alpha) = \epsilon \phi T^4 \quad (2)$$

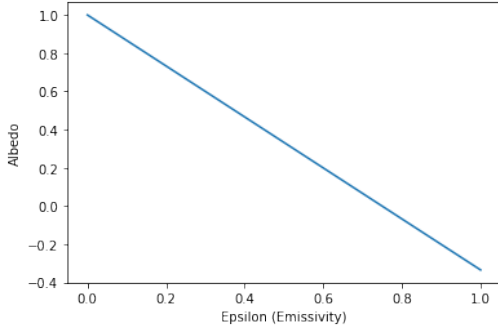


Figure 1: Albedo-Emissivity Profile

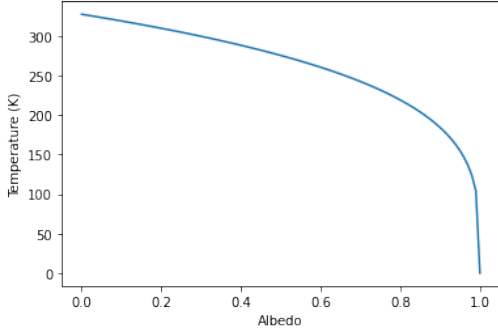


Figure 2: Temperature-Albedo Profile

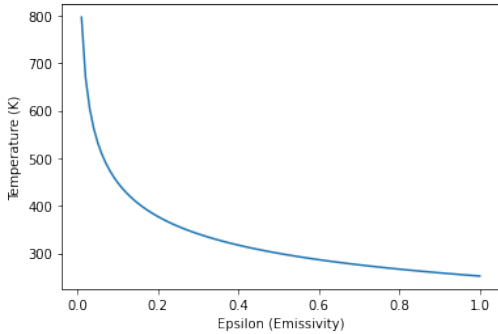


Figure 3: Temperature-Emissivity Profile

The two variables here (keeping with our model

output as constants), ϵ and α , can be plotted against each other as shown in Figure (1). If we approximate $\alpha \sim 0.3$ (as shown here [Stephens et al., 2015]), we can estimate $\epsilon \sim 0.524$. That being said, Earth's emissivity coefficient is much closer to unity than our calculated value. This is a result of atmospheric interference - particularly, the greenhouse effect - which has not been accounted for here. In general, the zero-dimensional model fails to accurately predict the Earth's radiating surface temperature. It is better suited to bodies that either have an inherently even energy distribution - such as the Moon - or energy transfer mechanisms efficient enough to maintain an even distribution. Note that the relationship between temperature and emissivity demonstrates that the surface converges to its blackbody temperature as the surface emissivity approaches unity.

3 The Goldilocks Zone

This section seeks to outline a strategy using to define a range of radii around an arbitrary star system that can house a terrestrial planet that supports liquid water. A rough assumption we make to meet this criterion is that the average surface temperature should lie between 220 K and 320 K. This approach builds on the methods described in the previous section on zero-dimensional modelling.

As explained in Section 1, the only energy source our system will consider is the solar irradiance. Similarly, the primary energy sink considered is the planet's outgoing radiation. The hypothesized planet will be optically similar to Earth's, allowing us to utilize experimentally-observed values in this procedure. Regarding the acceptable surface temperature interval - we expect a runaway greenhouse effect to take hold if temperature exceeds the 320 K limit [Nakajima et al., 1992], while a breach of the lower limit could result in a prolonged snowball state [Pierrehumbert, 2005]. The primary input quantity is solar luminosity, treated as a constant in this system. However, accommodations for variability would have to be made for a long-term observation in order to account for the changes in radiative intensity across the star's life cycle.

By the inverse square law applied to radiation,

$$\phi \propto \frac{1}{R^2} \quad (3)$$

where ϕ is solar irradiance and R is the radius we look to identify in this exercise.

Viewing ϕ as a measure of intensity, we can redefine it as a function of R in terms of power (luminosity) and surface area as follows:

$$\phi(R) = \frac{L_{\odot}}{4\pi R^2} \quad (4)$$

where L_{\odot} is the solar luminosity.

Therefore, we can use this function to model the incident radiative flux density on the surface and set up an equation (assuming a stable energy budget) to evaluate ϕ at a chosen surface temperature from our acceptable range. Although conventional models use the Stefan-Boltzmann law to estimate the planet's outgoing radiative flux density (σT^4), we will instead define this quantity with an arbitrary function that indicates atmospheric CO_2 mass as a parameter. This is to ensure that the influence of carbon dioxide is dealt with. However, modelling the radiative flux under these conditions is beyond the scope of this approach. Thus,

$$\frac{\phi}{4}(1 - \alpha) = OLR(T_e, CO_2) \quad (5)$$

where α is the planet's average surface albedo and $OLR(T_e, CO_2)$ is our function for outgoing radiative flux density. This approach requires further evaluation of the range of habitable radii using a selection of reasonable CO_2 masses to better understand the relationship between the two.

We use Equation (5) to identify the solar irradiance for a given equilibrium surface temperature (T_e) by restructuring (5) as follows:

$$\phi = \frac{4 \cdot OLR(T_e, CO_2)}{1 - \alpha} \quad (6)$$

To solve for ϕ , α can be estimated using the following analytical solution:

$$\alpha(T_e) = \alpha_i - (\alpha_i - \alpha_o) \frac{(T_e - T_i)^2}{(T_i - T_o)^2} \quad (7)$$

We now substitute a $\alpha(220K)$ approximation in (6) and solve for ϕ . In turn, this value for irradiance can be used to find R using (2). We repeat this procedure using $T_e = 320K$ to find the Goldilocks zone's lower limit. All intermediate radii belong to the zone and form our range of habitability.

The final product of the outline describes the habitable zone as a function of atmospheric CO_2 mass. Its influence on the position of the boundary radii can be explored empirically for reasonable estimations of carbon dioxide concentrations.

The significance of this problem is paramount. Identifying the regions around a star where planets can support liquid water is one of the first steps to narrowing the range of habitability to an extent that it can be explored adequately. Although most traditional methods to identifying the Goldilocks zone remain fairly crude in their assumptions, the imprecise nature of the problem lends itself to accommodating these estimations. Reasonable approximations alone allow for a feasibly narrow range of planets across numerous star systems that can be further explored to find traces of intelligent life.

4 Moving to 1D Models

The 1D model adds a vertical dimension to our previous 0D setup, implying the consideration of an atmosphere and a horizontal homogeneity assumption (as first suggested by [Meador and Weaver, 1980]) As Earth's atmosphere is transparent to shortwave radiation, we instead examine the impact of a striated atmosphere on the OLR component. If we consider a series of layers (of infinitesimal depth) in the atmosphere, we have to find the radiating temperature (T_e) of each layer (defined by δp) to compute the net upward flux leaving the system.

4.1 Optical Depth As A Vertical Coordinate

The equations governing radiative transfer become simpler when we adopt optical depth as the vertical coordinate in our system. The following section redefines optical depth in terms of pressure to create this conversion.

Assuming hydrostatic balance, $mg = \delta p$ for each layer. We can also define an absorption coefficient, κ that will depend upon the temperature and pressure of the layer, and the frequency of the incident radiation. An important association to make is that this coefficient is numerically equivalent to an emissivity coefficient, by Kirchhoff's thermal radiation law. Note that $\kappa_{\nu} = 0$ for solar radiation ($\lambda_{peak} \sim 500nm$), leading to the apparent transparency.

The following definitions allow us to utilize optical thickness as a vertical coordinate. This significantly simplifies following calculations, due to the direct relationship between radiation and optical depth.

$$\delta\tau_*(\nu, p, T) = -\kappa m = -\kappa \frac{\delta p}{g} \quad (8)$$

Equation (8) only applies for a ray normal to the layer's surface. To account for this, we can re-define optical thickness to account for angular changes.

$$\delta\tau = \frac{\delta\tau_*}{\cos\theta} = -\frac{\kappa m}{\cos\theta} = -\frac{k}{\cos\theta} \frac{\delta p}{g} \quad (9)$$

κ is directly dependent on the nature of the medium. As such, it cannot serve as a universal constant across the atmosphere since there is significant variability in its constituents at different altitudes. Therefore, a weighted average (by mass concentration) of each constituent is calculated individually for all observed levels:

$$\kappa(z) = \sum_i \kappa_i \frac{m_i}{\sum m_i} \quad (10)$$

4.2 The Schwarzschild Approximations

Consider a 'slab' (of height $\delta\tau$) of this striated atmosphere with a beam of intensity I incident on its lower surface. The absorbed radiative intensity can be modelled by the expression, $I\tau_*\delta\tau$. This is the product of the radiative intensity, the absorptivity coefficient, and the depth of the layer, respectively. The following equations will describe a non-scattering radiative transfer model. We can now set up an energy conservation equation as follows:

$$I\tau_*\delta\tau = (1 - \delta\tau_*)I + B\delta\tau_* \quad (11)$$

where $(1 - \delta\tau_*)I$ is the fraction of unabsorbed radiation and B is the blackbody radiation which is multiplied by $\delta\tau_*$ to define the radiative intensity emitted by the layer.

Calculating the net radiative upflux involves integrating (11) for the full angular dependence of the flux. Accounting for the conversion from spherical to Cartesian coordinates, the function must be integrated by $\int_0^{\frac{\pi}{2}} \int_0^\pi d\phi \cdot \sin\theta d\theta$. The inclusion of $\cos\theta$ on the right-hand side of Equation (11) complicates its mathematical solution, however. The average θ is approximated to $\pi/3$, and I is assumed to be isotropic in order to simplify the integration to the following estimations:

$$\frac{d}{d\tau_\nu} I_+ = -I_+ + \pi B(\nu, T(\tau_\nu)) \quad (12)$$

$$\frac{d}{d\tau_\nu} I_- = I_- - \pi B(\nu, T(\tau_\nu)) \quad (13)$$

where I_+ and I_- are the upward and downward fluxes respectively. Separating the net flux equation into these two components give rise to the two-stream Schwarzschild approximations.

To find functions for upwelling and downwelling radiative components, we convert these differential equations to their integral form. Since they are first-order ODEs, we take an integrating factor of $e^{-d\tau}$. Although the equations above describe radiative flux as a function of frequency, we define a function for monochromatic radiation to simplify our calculations. As such, τ must be appropriately adjusted if multiple frequencies are used. The function for upwelling radiation (I_+) is as follows. Since ν is no longer considered, it is no longer a parameter of the blackbody function, and τ is no longer shown with a ν suffix.

$$I_+(\tau) = I_+(0)e^{-\tau} + \int_0^\tau \pi B(T(\tau'))e^{-(\tau-\tau')}d\tau' \quad (14)$$

There are 2 sources shown here. The first term describes incident radiation from a level at $\tau = 0$ (the planet's surface). It is multiplied by an attenuation coefficient, $e^{-\tau}$, which accounts for the loss of flux intensity as the radiation passes through optically thick layers to reach the height τ . Note that the coefficient is maximized when τ is low, demonstrating that the loss in intensity falls with height. The second term integrates the emitted radiation from all levels between the surface and the observed height. This term also contains an attenuation coefficient ($e^{-(\tau-\tau')}$) that accounts for the loss in intensity between the observed and intermediate heights. The attenuation coefficients play a role in determining the function's sensitivity to different layers' outputs. Consider the example $I_+(\tau_\infty)$ - which would model the planet's OLR. In this case, the surface output's attenuation coefficient, $e^{-\tau_\infty}$, reduces its output to a negligible value. Conversely, the atmospheric output is least diminished when $\tau - \tau'$ is close to zero, i.e. $\tau' \rightarrow \tau_\infty$. Therefore, the final output of the function is far more sensitive to upper-layer influence.

The function for downwelling radiation (I_-) takes a similar approach and is shown below.

$$I_-(\tau) = I_-(\tau_\infty)e^{-(\tau_\infty-\tau)} + \int_\tau^{\tau_\infty} \pi B(T(\tau'))e^{-(\tau-\tau')}d\tau' \quad (15)$$

The first term often carries a null value. This is because we distinguish between fluxes of different frequencies: longwave radiation at NTAT is not expected to be incident on the planet, while insolation is. Therefore, we expect $I_-(\tau_\infty) = 0$ when examining interactions between the atmosphere and the surface. The second term accounts for all downwelling back-radiation emitted by the atmosphere towards the surface. As seen in (14), its attenuation coefficient increases radiative in-

fluence with τ' proximity to τ .

Extending these equations to gaseous planets involves identifying a level in the atmosphere that is sufficiently dense to ensure the body lying underneath acts as a blackbody. This is a requirement for the upwelling equation since τ_0 is not clearly defined in this context.

The computational implementation of these equations adjusts τ_∞ to a level that is sufficiently optically-thin such that further layers do not significantly affect key metrics eg. OLR. There are two potential cases where a level meets this criteria. The first is that the atmospheric constituents at that level have negligible opacity (with regards to the radiative frequency). The more likely case is that the pressure is acceptably low such that interactions with radiation are infrequent enough that the layer is roughly transparent. Although, the altitude of the 'boundary' layer is likely to change across different frequencies.

5 A 1D Radiative Transfer Model

The grey gas model assumes that the atmosphere is transparent to insolation and has an absorption coefficient that remains constant throughout the medium for a given frequency band. By extending our model with a vertical component, we now begin to observe the atmospheric effects on OLR, primarily (since we assume transparency to solar radiation). Note that this is a non-scattering radiative model. This section will also focus on relationships between optical thickness, optical depth, absorptivity, net radiative flux, and pressure. Note that we will refer to optical 'thickness' as a measure of the entire atmosphere's optical effects, while optical 'depth' will refer to a vertical coordinate.

In addition to the libraries introduced in Section 2, this model uses `metpy` [May et al., 2017]. This module is often used in weather-based applications and will aid in forming a reasonable temperature profile. We assume a fairly arbitrary surface temperature and initialize the `GrayLongwaveRadiation` component from `CLiMT`. We redefine the air temperature quantities in our model state using `metpy`'s dry lapse function, while accounting for the fall in temperature on the atmosphere-surface boundary. We also set a fairly arbitrary value for τ_∞ and a linear coefficient (relating to the absorptivity through the medium) of 0.1. We adjust the state's optical depth property in lines 18-21 to

account for our new value of τ_∞ . Lastly, we simplify the optical depth and air pressure (in kPa) state variables to use as vertical coordinates.

5.1 Vertical Coordinates

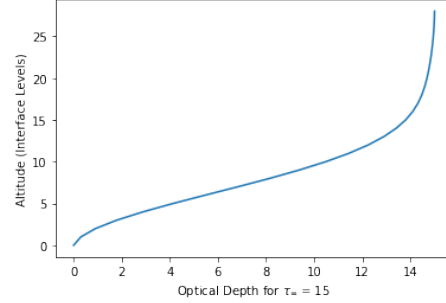


Figure 4: τ Vertical Profile

This section looks at optical depth, air pressure to provide an understanding of the relationships between the 3, and demonstrates the usage of pressure and optical depth as vertical coordinates. Altitude is measured as a series of interface levels. Note that these intervals are not evenly-spaced; they are adjusted to provide a clearer view of changes in the system. All plots here were created using the model setup shown earlier. We have modelled a fairly optically-thick atmosphere here : $\tau_\infty = 15$.

Figure 4 shows optical depth appearing to increase in a reasonably stable manner till the 13th interface level, implying similar absorptive properties in lower layers. The spike shown at higher levels of optical depth shows that these upper layers are relatively optically-thin: they show little increase in aggregate optical depth for a large increase in altitude. Therefore, absorptivity appears to roughly fall with altitude. This graph, however, does not inform us as to whether this is a result of a change in pressure, temperature or substance-specific absorptive properties across height. The former two certainly play a role, but the extent of their impact cannot be resolved here.

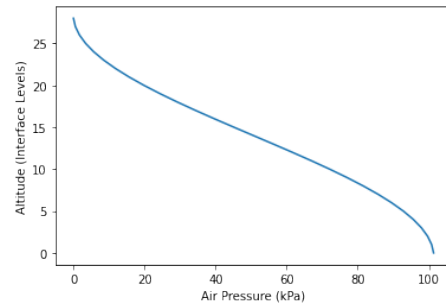


Figure 5: Air Pressure Vertical Profile

Figure 5 shows the relationship between air pressure and altitude. Pressure falls exponentially with altitude, but the uneven spacing between intervals leads to a more linear relationship.

5.2 Variation in Longwave Optical Depth Profiles

The different profiles in Figure 6 highlight the changes in absorptive properties for atmospheres of varying optical thicknesses. Pressure is used as a vertical coordinate in this graph, with a reversed y-axis to account for its inverse relationship with altitude. Note that the `linear` parameter in the optical depth function has been kept constant.

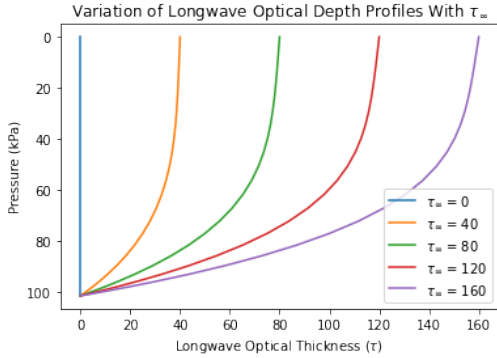


Figure 6: Longwave optical depth - pressure profiles for a range of τ_∞ values

Across all non-transparent profiles, we see a sharp increase in optical depth near the surface, which soon decreases to a constant. The exponential fall in τ is most likely driven by the similar decrease in temperature and pressure across altitude. The height at which $\frac{d\tau}{dp}$ reaches 0 (i.e. aggregate optical depth reaches τ_∞) is significant. There is no absorption past this level, so the upwelling longwave radiation here is numerically equal to the planet's OLR- and is thus referred to as the system's radiating height. The graph shows that this level increases with τ_∞ .

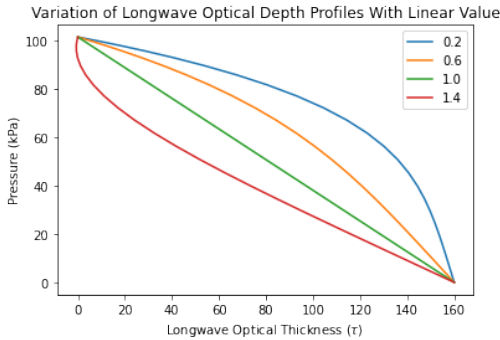


Figure 7: Longwave optical depth - pressure profiles for a range of `linear` values.

Figure 7 allows us to derive a simple relationship

between the absorptivity coefficient (κ) and altitude. For `linear` values less than 1, we observe that

$$\frac{d^2\tau}{dp^2} < 0 \Rightarrow \frac{1}{g} \frac{d}{dp}(-\kappa) < 0 \Rightarrow \frac{d\kappa}{dp} > 0$$

We use Equation (8) in the expression above. $\frac{d\kappa}{dz} = \frac{d\kappa}{dp} \frac{dp}{dz}$, by the chain rule. We know $\frac{dp}{dz} < 0$ from the hydrostatic equation [Wallace and Hobbs, 2006]. Therefore, the product shown takes on a negative value, so we can show that the absorptivity coefficient falls with height.

For the `linear` value of 1, we see a constant gradient, implying the second derivative of τ with respect to p is 0. Similar deductions show that the absorptivity coefficient is constant ($\frac{d\kappa}{dz} = 0$). In this case, the model displays a gray gas approximation, where absorption is uniform throughout the medium. A `linear` value greater than one implies an absorptivity coefficient that increases with height.

5.3 Flux Divergence Profiles

Flux divergence (or, net flux) is defined as the difference between upwelling and downwelling radiation (of a single frequency) at a given altitude. Using the Schwarzschild approximations, we can define it as $I_+(\tau) - I_-(\tau)$. The flux divergence profile can also be used to find a function for heating rate - it is simply the derivative of flux divergence with respect to optical depth. The following section evaluates flux divergence using the pressure and optical depth coordinates.

Our function uses τ_∞ and the `linear` value as parameters, in order to find the vertical optical depth profile. A grey gas component is applied to the model to calculate the upwelling and downwelling longwave fluxes to calculate flux divergence as a function of optical depth. The parameters used to produce the following graphs from the function in Figure 11 are kept constant - a τ_∞ of 160, and a `linear` value of 0.1. This ensures a reasonably optically-thick atmosphere, with a falling absorptivity coefficient (with respect to altitude), respectively.

Our `linear` value was set to its default value of 0.1, so our optical depth profiles show that the absorptivity coefficient used here falls with height. Therefore, the back radiation flux density from absorbed radiation is expected to fall with optical depth, and the undisturbed upwelling flux density increases. The spike seen towards the upper can be explained by the lower absorptivity at higher altitudes, given that pressure and temper-

ature fall, leading to a higher net flux. It is likely that the deflection would occur at a lower altitude for an optically-thinner atmosphere. The following drop can be explained by stratospheric action, where a temperature inversion could be a result of a fall in net flux.

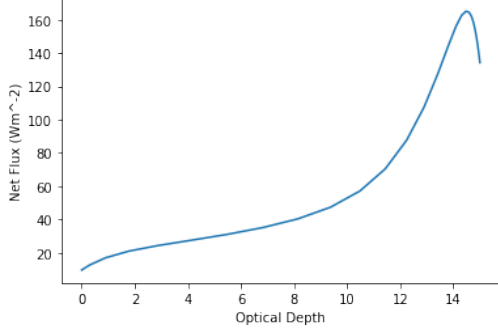


Figure 8: Net Flux, Vertical Profile (Optical Depth)

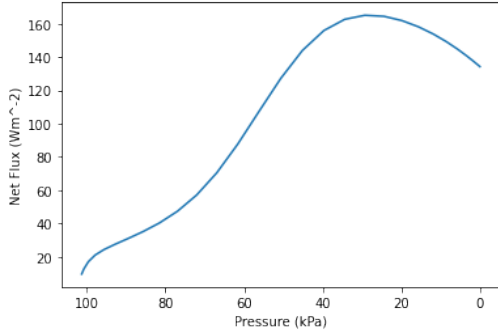


Figure 9: Net Flux, Vertical Profile (Air Pressure, kPa)

Figure 9 provides us with further evidence of stratospheric influence reducing net flux, seeing as the graph appears stationary at the 20 kPa height- which is reasonably close to the average height of the tropopause.

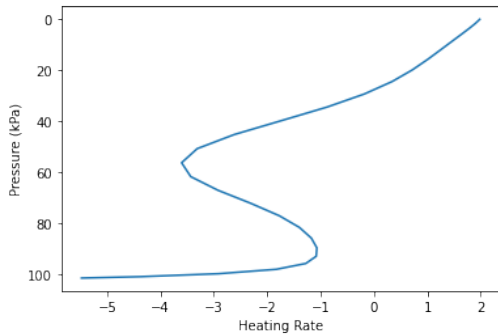


Figure 10: Heating Rate, Vertical Profile

Figure 10 describes the heating rate in the atmosphere with respect to pressure. The extreme cooling seen near the surface is a result of the sudden increase in radiation, primarily driven by the temperature gradient across the surface-atmosphere boundary. It soon stabilizes, reduc-

ing the cooling at higher altitudes, given that the fall in temperature across atmospheric levels is far lower than the surface-boundary drop. Past the tropopause, we begin to see a positive heating rate, likely due to stratospheric heating- which reduces the back radiative flux. Note that the heating rate profile describes a direct relationship with the vertical temperature profile. Therefore, the heat capacity of most constituents remain roughly similar, since the mass factor is taken to be constant when we use a pressure profile. The figure also provides evidence for disequilibrium: a thermally-stable would see negligible heating rates, at all altitudes.

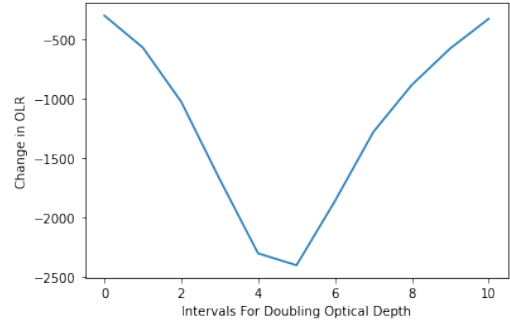


Figure 11: Change in outgoing longwave radiative flux for a doubling of τ_{∞} , from 0.05 to 102.4.

We see a general fall in OLR with an increase in the optical thickness of the atmosphere. However, the extent of this fall varies across the range observed. The greatest decrease in OLR is seen at the 5th interval i.e. $\tau_{\infty} = 1.6$. For optically-thinner atmospheres, the change in OLR is lower since atmospheric absorption (and thus, emission) has less influence. Thicker atmospheres see a lower change in OLR since the increased absorptivity likely increases the back-radiative percentage of incident radiation, primarily at lower altitudes.

5.4 Isothermal Profiles

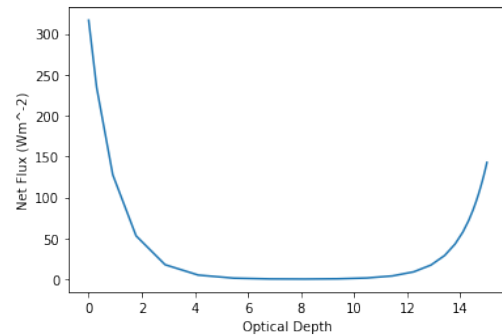


Figure 12: Isothermal Net Flux, Vertical Profile (Optical Depth)

This section evaluates flux divergence given isothermal vertical temperature profiles. We set an atmospheric temperature equal to the average of the default profile. As in section 5.3, both a pressure-vertical profile and an optical depth-vertical profile are used.

As expected, much of the atmosphere sees no net flux, implying that the back radiation and upwelling radiation are equal, due to the lack of any vertical temperature gradient. However, there is a high upward flux at the surface, seen as a result of the temperature gradient at the surface-atmosphere boundary. The net upward flux towards the upper layers of the atmosphere are a result of stratospheric activity. An isothermal approximation would increase the upwelling radiative intensity to counter the release of energy in the ozone cycle.

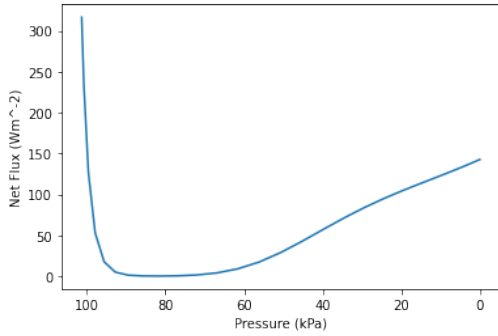


Figure 13: Isothermal Net Flux, Vertical Profile (Pressure)

6 A 1D Radiative Equilibrium Model

The chief differentiator between this model its predecessors is the integration of time as a dimension over which the system comes to equilibrium, ensuring long-term stability. Therefore, an additional variable that requires consideration is the time taken by the system to approach equilibrium. All other variables have been presented either using their changes in the months approaching equilibrium or their stable-system vertical profile. We maintain the same spatial restrictions used in Section 5. Note that the model only uses radiative transfer for energy transport; not convection.

This system consists of 2 components: a black-body slab surface and an atmospheric column above it. The energy fluxes at the atmospheric boundaries are monitored as a criterion for equilibrium. We assume large-scale stability when the net energy level in the atmosphere is zero i.e.

the sum of the upwelling and downwelling fluxes at the ground and the top of the atmosphere, of both shortwave and longwave radiation, is zero.

The model's initial conditions are as follows: an average surface albedo of 0.3, a vertically-uniform insolation flux of 200 W/m^2 , a surface temperature of 300 K, and a vertically-uniform air temperature of 200 K, and an energy budget error margin of 0.5 W/m^2 , and a longwave optical depth of 6. The model takes 259.67 days to reach equilibrium, using 4-hour time increments. It uses CLiMT's implementation of the Adams-Bashforth numerical integration technique [Durran, 1991] to step the model forward in time.

6.1 Weekly Long-term Profiles

This section looks at the evolution of certain 0d variables involved in our model as they approach equilibrium. The data was saved on a weekly basis to create these profiles.

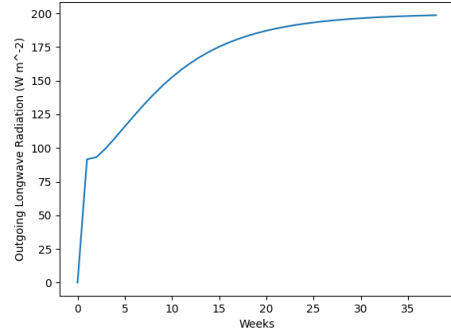


Figure 14: Weekly OLR Profile

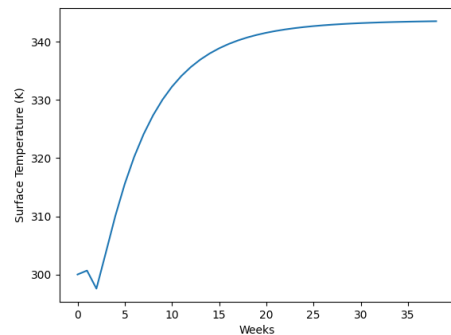


Figure 15: Weekly Surface Temperature Profile

As expected, the planet's OLR (see Figure 14) converges to a singular value (199.8 W/m^2) as the system approaches equilibrium. Similarly, the surface temperature (see Figure 15) converges to a value of 343.5 K. The model describes a planet at a surface temperature high enough that it could undergo a runaway greenhouse ef-

fect, and therefore fails to accurately describe Earth's climate. This is primarily caused by only considering radiative transfer as an energy transport mechanism and thus, disregarding convection's role in mediating vertical temperature profiles through latent and surface heat fluxes.

The rapid fall from a 100 K (set up by the model's initial conditions) to a 12.4 K difference in Figure 16 is driven by the surface's longwave emission. Note that the atmospheric temperature measured here is that of the lowest interface level. The speed at which the profile reaches stability also suggests that the surface's radiative cooling as the primary factor for the atmosphere's heating. Therefore, the introduction of convection as an energy transport mechanism would likely alter this speed.

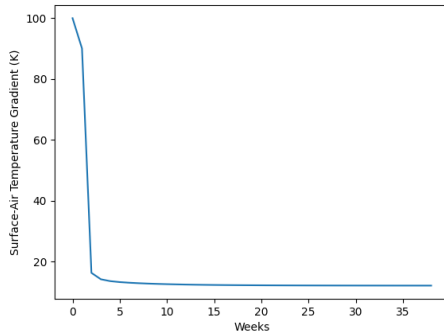


Figure 16: Weekly Atmosphere-Surface Temperature Gradient Profile.

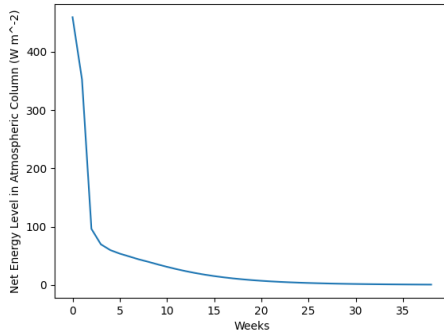


Figure 17: Weekly measurements of the net energy level in the atmospheric column.

Figure 17's variable acts as the model's chief stopping criterion. The program terminates when the net energy level in the atmospheric column stabilizes to a value within a reasonable error margin. The delayed fall seen in Figure 17 points to a relatively inefficient mode of energy transport involved in radiative equilibrium. The cause identified here is the upwelling radiation from upper layers in the atmosphere: the lower absorptivity at these altitudes (due to the fall in pressure)

restricts their ability to emit at a constant, stable radiative temperature. The dependency on energy input from relatively inefficient layers beneath further develops this time lag.

6.2 Equilibrium Profiles

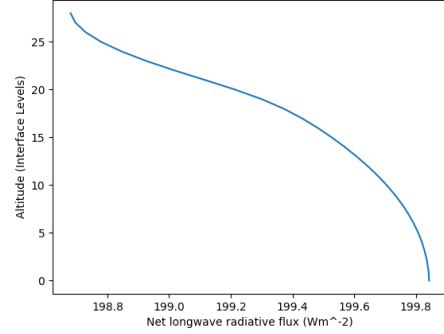


Figure 18: Longwave Flux Divergence Vertical Profile (Interface Levels) At Equilibrium

Figure 18 demonstrates that the variation in longwave net flux across its vertical scale is fairly minute, as is to be expected for a stable system. Large imbalances in flux divergence would imply strong heating rates at certain altitudes. The resulting variation in temperature could prevent the stability of a vertical optical depth, given the direct relationship between the two- which further restricts flux divergence stability. Thus, we can reasonably assume the equilibrium state is directly dependent on a relatively uniform vertical longwave flux divergence profile. A constant flux divergence value could serve as a marker for the system's idealized value. Our stopping criterion allowed a 0.5 W/m^2 net energy level in the atmospheric column to mimic the Earth system, seeing as it remains only close to equilibrium, resulting in the difference in flux divergence seen across the atmospheric column boundaries.

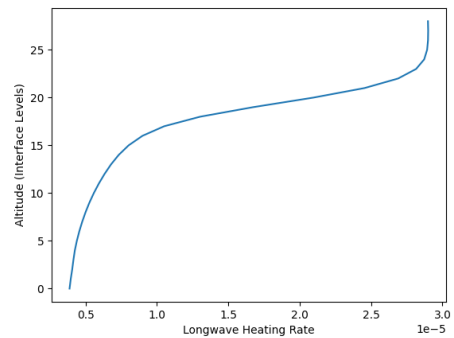


Figure 19: Heating Rate, Vertical Profile (Interface Levels) At Equilibrium

As mentioned earlier, a prerequisite for stability is a low-to-negligible heating rate across its

vertical profile. Figure 19 exhibits this, considering its 10^{-5} x-scale. The heating rate would be zero at all heights, keeping with our constant flux divergence value for idealized equilibrium.

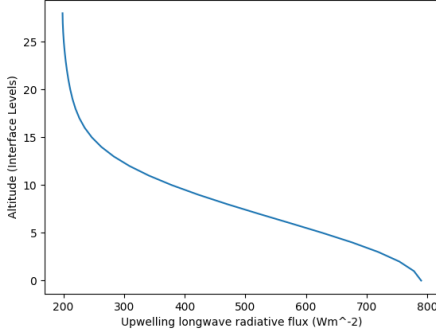


Figure 20: Longwave Upwelling Radiative Flux, Vertical Profile (Interface Levels) At Equilibrium

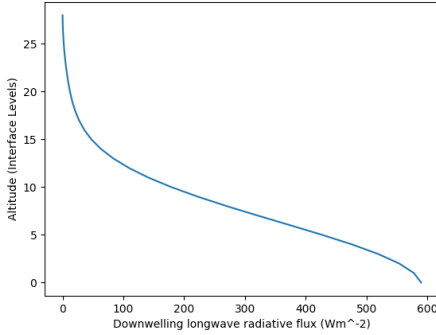


Figure 21: Longwave Downwelling Radiative Flux Vertical Profile At Equilibrium

As expected, the higher absorptivity at lower altitudes drastically reduces their longwave upwelling radiative flux. This effect falls with an increase in altitude, leading the radiative flux to stabilize $\sim 199 \text{ W/m}^2$. A significant quantity that can be calculated using this profile is the planet's effective radiating altitude/pressure level. Upper atmospheric layers have lower absorptivity, and therefore become increasingly transparent to longwave radiation. Therefore, their attenuative influence can be disregarded. We can identify a suitable radiating height at equilibrium by allowing a reasonable error margin (difference between the the slab's upwelling longwave flux and the planet's OLR). For an error margin of 0.5 W/m^2 , the model's radiating height is the 24th interface level, or 18 kPa (Figure 5). The computational implications of identifying a suitable radiating height are paramount: although a low radiating height offers significant runtime benefits, an aggressive error margin could hamper the accuracy of model results. The usage of a radiating altitude in cal-

culations is only applicable to stable states, and was not used in creating any of the weekly-long term profiles.

The similarity between the longwave upwelling and downwelling flux profiles (separated by a phase difference) creates the vertically-stable flux divergence profile in Figure 18. Just as the upwelling profile was explained by changes in absorptivity over height, Figure 21 is also a result of the equilibrium optical depth vertical profile. The back-radiation from low-altitude atmospheric components creates the spike in downwelling radiative flux near the surface. As absorption falls with altitude, the back-radiation falls.

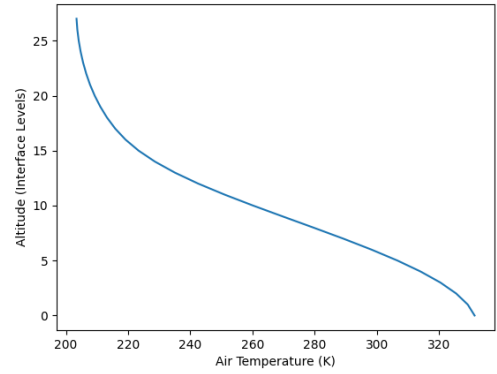


Figure 22: Air Temperature, Vertical Profile (Interface Levels) At Equilibrium

The model outputs a reasonably accurate representation of the Earth's vertical temperature profile, especially at upper altitudes. Given the uneven spacing between interface levels, Figure 22 appears to mimic the typical exponential fall in temperature suggested by the radiative equilibrium model. However, most observations conclude a linear lapse rate [Manabe and Wetherald, 1967] in the troposphere that fails to be seen here. This is primarily caused by the instability that a purely radiative system creates at lower altitudes. The significant temperature gradients in the lower boundary region causes intense radiative cooling that destabilizes the system.

6.3 Instability Duration And Optical Thickness

Figure 23 looks at the duration of instability in the system before it reaches equilibrium for a range of τ_∞ values.

In general, for optically-thin atmospheres ($\tau_\infty \ll 1$), this timespan is fairly short. This can be explained by the relatively minute role of

the atmosphere. Since its average absorptivity is lower, the planet acts increasingly as a black-body, where the only relevant outgoing source is the surface. In general, atmospheric influence tends to be less efficient than the surface, and thus, extends the instability duration. Thus, when its role is diminished, the model reaches equilibrium faster. It follows that the increasing timespan for optically-thicker systems is a result of greater atmospheric influence.

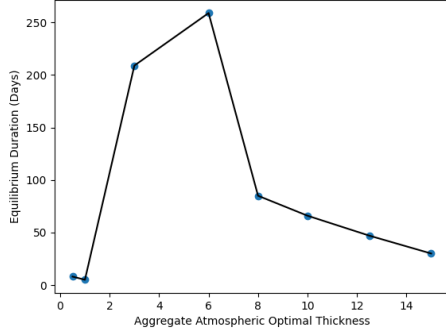


Figure 23: A scatterplot describing the time the model takes to take to come to equilibrium for a range of aggregate optical thicknesses.

However, the graph also describes a sharp drop in the instability duration for extremely optically-thick atmospheres. In these cases ($\tau_{\infty} \gg 1$), most of the relevant observed atmospheric layers have an optical thickness high enough to absorb a significant fraction of upwelling radiation from below. Therefore, the longwave flux (in either direction) at any given height is primarily a result of the emission from that 'slab', as opposed to unabsorbed radiation from lower layers. We can consider the flux at each of these layers independent of lower ones. Thus, they act as locally isothermal slabs, each radiating at a given temperature. As seen in exercises for an isothermal atmosphere, these layers act ideally as blackbodies. This lowers the instability duration.

7 A 1d Radiative-Convective Equilibrium (RCE) Model

One of the major caveats of the radiative equilibrium model is that it fails to take into account the static instability in boundary layers [Held, 1982]. The RCE model is designed to account for this instability by employing convection as a mechanism to transport sufficient heat upwards from the surface, when the lapse rate passes a critical value of $6.5^{\circ}\text{Ckm}^{-1}$ [Manabe and Wetherald, 1967]. This critical value is a result of both the stabilizing effects of upward energy trans-

fer via convective thermals and the destabilizing effect of radiative transfer [Manabe and Strickler, 1964]. This chapter looks to describe the effect that this convective component has on the profiles that make up the bulk of Section 6. The model's initial conditions are identical to those of the radiative equilibrium model, except an atmospheric optical thickness of 8. Our RCE model runtime is lower than its counterpart: 163 days. We employ smaller (1-hour) time increments to account for the stronger variation of convective processes.

The equilibrium flux divergence profile for the RCE model had similar results as in the radiative equilibrium model: there was a deviation of 0.8 W/m^2 across the atmospheric boundaries with the value remaining roughly constant for all vertical coordinates. Therefore, the RCE heating rate profile was similar to its radiative counterpart as well i.e. close to zero at all pressure levels.

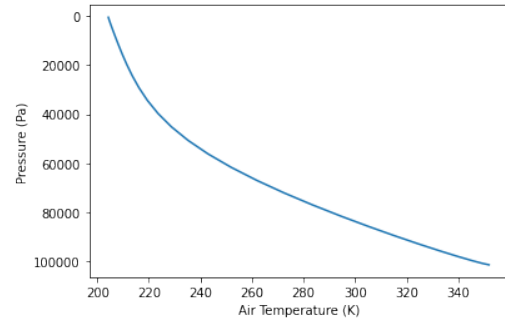


Figure 24: Equilibrium Air Temperature Profile, RCE Model

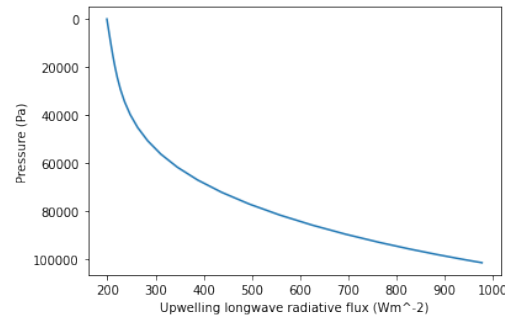


Figure 25: Equilibrium Longwave Upwelling Radiative Flux Profile, RCE Model

Figure ?? highlights the effect of convective action on the system's longwave fluxes and air temperature profile. The air temperature appears to fall in a linear fashion from the surface to $\sim 55 \text{ kPa}$, after which it falls exponentially. The divide shown here can be explained by convection's role as a cooling agent. Near the surface, the critical lapse rate breach stimulates convection, reducing the radiative cooling to a stable - and

thus, linear - rate. The temperature inversion near the tropopause prevents the vertical motion of aerosols that carry out convection. Convective cooling does not function past the troposphere, leading to the exponential fall in temperature. Therefore, the turning point between the linear and exponential section of the graph could represent an averaged tropopause height.

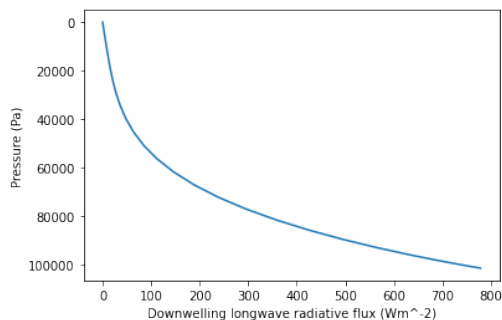


Figure 26: Equilibrium Longwave Downwelling Radiative Flux Profile, RCE Model

Figures 25 and 26 tell a similar story, both showing a capped lapse rate in the troposphere. As in radiative equilibrium - their ideal values are separated by a constant value $\sim 200 \text{ W/m}^2$ - creating a vertically-stable flux divergence profile.

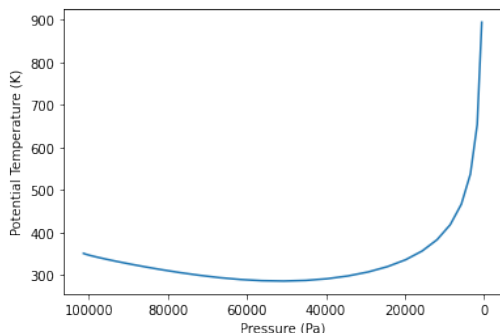


Figure 27: Equilibrium Potential Temperature Profile, RCE Model

metpy's potential temperature (Θ) function is leveraged across all interface levels of the model to generate Figure 27. If potential temperature were to increase with height (i.e. $\frac{d\Theta}{dz} > 0$), adiabatically-raised air parcels would be cooler than those at lower altitudes. Being denser, they would sink, creating a statically-unstable atmosphere. Conversely, a statically-stable atmosphere would show a fall in potential temperature with height.

Our potential temperature profile shows $\frac{d\Theta}{dz} > 0$ from the surface to the 55 kPa pressure level. Therefore, the atmosphere is statically-unstable in this range, and convection can act as a heating mechanism. The increase in the graph's gradient towards 45 kPa in this range points to an

increasing stability at higher altitudes. This suggests that convection's role, although serviceable to the tropopause, diminishes at higher levels. Conversely, $\frac{d\Theta}{dz} < 0$ from the 55 kPa pressure level to NTAT, so no convection takes place.

Summary

The ability to model climate to a reasonable degree of accuracy is a significant tool in aiding our understanding and predictability of mean climate behaviour. We began with the examination and elimination of potential energy sources and sinks that allow us to begin to construct models. Considering that our area of interest lies primarily in the lithosphere and atmosphere, we concluded that insolation and emitted radiation from the planet were the only viable energy source and sink, respectively.

This report outlined 3 major approaches to modelling planetary energetics: 0d models, a radiative equilibrium model, and an RCE model. Each presented their own caveats with regard to accuracy, seeing as they highlighted specific assumptions that hampered their precision. For example, all models assumed hemispheric symmetry of insolation.

Ignoring atmospheric interference reduced Section 2's 0d model's estimated surface emissivity coefficient to 0.524, although it exhibits near-blackbody behaviour in reality. The radiative equilibrium model created energy gradients in the lower boundary layers that led to exponential lapse rates in the troposphere. Our RCE model corrected for this instability, but it lacked the complexity to account for significant variation in energetics caused by factors like aerosol formation, wind and ocean transfer, etc. That being said, it appears to reach reasonable estimations of a diurnally- and seasonally- averaged Earth profile.

One area of interest that remains unanswered by this report is the variance of the models' profiles across x-y coordinates. All models used cosine weighting to develop point-based or line-based coordinate systems. As a result, its validity with regards to a latitudinal-longitudinal system is yet to be explored.

The techniques used in developing the 0d model were leveraged to outline a strategy that could help identify the region of habitability around a star of a given luminosity (the Goldilocks problem). The simple approach applied the inverse square law to radiation in order to determine the

intensity of a beam on a planetary surface. We set up an energy balance equation for a system in equilibrium, allowing us to account for albedo, average surface temperature, and atmospheric CO₂ levels. Our α function leveraged snowball techniques to reach an analytical solution for the planet’s albedo. It classified any y-coordinate as ice-free or in a snowball state, depending on its surface temperature. Using cosine weighting, the binary latitudinal outputs were averaged to reach a singular average planetary albedo. We have not explored the accuracy of this function with respect to Earth’s seasonal and diurnal variations, and remains an interesting area for further discussion.

This report (Section 5) also examined the relationships between optical depth profiles, pressure, atmospheric optical thickness, flux divergence, and OLR. However, their examination when at equilibrium would provide a more complete understanding of these relationships.

References

- [Archer, 2011] Archer, D. (2011). *Global warming: understanding the forecast*. John Wiley & Sons.
- [Camuffo, 2001] Camuffo, D. (2001). Lunar influences on climate. In *Earth-Moon Relationships*, pages 99–113. Springer.
- [Condie, 2013] Condie, K. C. (2013). *Plate tectonics & crustal evolution*. Elsevier.
- [Durrán, 1991] Durrán, D. R. (1991). The third-order adams-bashforth method: An attractive alternative to leapfrog time differencing. *Monthly weather review*, 119(3):702–720.
- [Ernst et al., 2016] Ernst, W., Sleep, N. H., and Tsujimori, T. (2016). Plate-tectonic evolution of the earth: bottom-up and top-down mantle circulation. *Canadian Journal of Earth Sciences*, 53(11):1103–1120.
- [Held, 1982] Held, I. M. (1982). On the height of the tropopause and the static stability of the troposphere. *Journal of the Atmospheric Sciences*, 39(2):412–417.
- [Holopainen, 1963] Holopainen, E. O. (1963). On the dissipation of kinetic energy in the atmosphere 1. *Tellus*, 15(1):26–32.
- [Johnson, 1954] Johnson, F. S. (1954). The solar constant. *Journal of Atmospheric Sciences*, 11(6):431–439.
- [Lenardic et al., 2005] Lenardic, A., Moresi, L.-N., Jellinek, A., and Manga, M. (2005). Continental insulation, mantle cooling, and the surface area of oceans and continents. *Earth and Planetary Science Letters*, 234(3-4):317–333.
- [Manabe and Strickler, 1964] Manabe, S. and Strickler, R. F. (1964). Thermal equilibrium of the atmosphere with a convective adjustment. *Journal of Atmospheric Sciences*, 21(4):361–385.
- [Manabe and Wetherald, 1967] Manabe, S. and Wetherald, R. T. (1967). Thermal equilibrium of the atmosphere with a given distribution of relative humidity.
- [May et al., 2017] May, R., Arms, S., Marsh, P., Bruning, E., Leeman, J., Goebbert, K., Thielen, J., and Bruick, Z. (2017). Metpy: A python package for meteorological data. *Unidata, Accessed*, 31.
- [Meador and Weaver, 1980] Meador, W. and Weaver, W. (1980). Two-stream approximations to radiative transfer in planetary atmospheres: A unified description of existing methods and a new improvement. *Journal of Atmospheric Sciences*, 37(3):630–643.
- [Monteiro and Caballero, 2016] Monteiro, J. M. and Caballero, R. (2016). The climate modelling toolkit. In *Proceedings of the 15th Python in Science Conference*, pages 69–74.
- [Monteiro et al., 2018] Monteiro, J. M., McGibbon, J., and Caballero, R. (2018). sympl (v. 0.4. 0) and climt (v. 0.15. 3)—towards a flexible framework for building model hierarchies in python. *Geoscientific Model Development*, 11(9):3781–3794.
- [Nakajima et al., 1992] Nakajima, S., Hayashi, Y.-Y., and Abe, Y. (1992). A study on the “runaway greenhouse effect” with a one-dimensional radiative-convective equilibrium model. *Journal of Atmospheric Sciences*, 49(23):2256–2266.
- [Pierrehumbert, 2005] Pierrehumbert, R. T. (2005). Climate dynamics of a hard snowball earth. *Journal of Geophysical Research: Atmospheres*, 110(D1).
- [Stephens et al., 2015] Stephens, G. L., O’Brien, D., Webster, P. J., Pilewski, P., Kato, S., and Li, J.-l. (2015). The albedo of earth. *Reviews of geophysics*, 53(1):141–163.
- [Turcotte and Schubert, 2002] Turcotte, D. L. and Schubert, G. (2002). *Geodynamics*. Cambridge university press.
- [Wallace and Hobbs, 2006] Wallace, J. M. and Hobbs, P. V. (2006). *Atmospheric science: an introductory survey*, volume 92. Elsevier.